Phys Chem Minerals (2000) 27: 270–284

ORIGINAL PAPER

A. Kirfel · G.V. Gibbs

Electron density distributions and bonded interactions for the fibrous zeolites natrolite, mesolite and scolecite and related materials

Received: 10 May 1999 / Revised, accepted: 14 September 1999

Abstract For the fibrous zeolites natrolite, $Na_2[Al_2Si_3O_{10}]\cdot 2H_2O$, mesolite, $Na_2Ca_2[Al_2Si_3O_{10}]_3\cdot 8H_2O$, and scolecite, $Ca[Al_2Si_3O_{10}]\cdot 3H_2O$, with topologically identical aluminosilicate framework structures, accurate single-crystal X-ray diffraction data have been analyzed by least-squares refinements using generalized scattering factor (GSF) models. The final agreement indices were $R(F) = 0.0061, 0.0165$, and 0.0073, respectively. Ensuing calculations of static deformation $[\Delta\rho(\mathbf{r})]$, and total, $[\rho(\mathbf{r})]$, model electron density distributions served to study chemical bonding, in particular by topological electron density analyses yielding bond critical point (bcp) properties and in situ cation electronegativities. The results for 32 SiO, 24 AlO, 14 CaO, and 12 NaO unique bonds are compiled and analyzed in terms of both mean values and correlations between bond lengths, bonded oxygen radii, bcp densities, curvatures at the bcps, and electronegativities. Comparison with recent literature data obtained from both experimental electron density studies on minerals and model calculations for geometry-optimized molecules shows that the majority of the present findings conforms well with chemical expectation and with the trends observed from molecular modeling. For the SiO bond, the shared interaction is indicated to increase with decreasing bond length, whereas the AlO bond is of distinctly more polar nature, as is the NaO bond compared to CaO. Also, the observed ranges of the Si and Al in situ electronegativities and their mean electronegativities agree well with both Pauling's values and model calculation results, and statistically significant correlations are obtained which are consistent with trends described for oxide and nitride molecules.

A. Kirfel (✉)
Mineralogisch-Petrologisches Institut
Poppelsdorfer Schloss, 53115 Bonn, Germany
e-mail: kirfel@uni-bonn.de
Fax: +49-228 73-2760

G.V. Gibbs
Department of Geological Sciences and Materials Sciences and Engineering and Mathematics,
Virginia Tech, Blacksburg, Virginia 24061, USA

Key words Electron density · Topological analysis · Zeolites

Model and observed bond critical point properties – review

The electron density distribution, $\rho(\mathbf{r})$, of a bonded array of atoms in a stationary state adopts an arrangement whereby the total energy of the resulting configuration is minimized. As is well known, two-dimensional contour maps of such a distribution in planes through the nuclei of the bonded atoms usually display well-defined maxima interconnected by a system of low-lying ridges. The maxima define the positions of the atoms while the ridges are features of the distributions that are related to the bonded interactions between the atoms (Bader 1998). Among the assorted properties of the distribution, the line that runs along the top of a ridge is special in the sense that it tends to follow a line in the distribution along which $\rho(\mathbf{r})$ is maximum relative to any neighboring line. As this line connects pairs of atoms that are assumed to be bonded (Bader and Essén 1984), it is referred to as the bond path. In general, the value of $\rho(\mathbf{r})$ decreases in a regular way along the path to a minimum value at a point between the atoms, referred to as the bond critical point, $(\mathbf{r}_c)$, where $\Delta\rho(\mathbf{r}) = 0$. According to Bader (1998), the presence of a bond path linking a pair of atoms provides a universal indicator of bonding between the atoms. Furthermore, the character of the bonding is concluded to be closely connected to the value of the electron density $\rho(\mathbf{r}_c)$ and the properties of the Laplacian of $\rho(\mathbf{r}), \nabla^2\rho(\mathbf{r}_c)$, both evaluated at $\mathbf{r}_c$ (Bader and Essén 1984). As observed by Bader (1990), by solving for the eigenvalues and eigenvectors of the Hessian matrix of $\rho(\mathbf{r}_c), H_{i,j} = \partial^2\rho(\mathbf{r}_c)/\partial x_i \partial x_j$, $(i, j = 1, 3)$, evaluated at $\mathbf{r}_c$, one obtains a diagonal matrix $\mathbf{\Lambda}$, whose trace equals $\nabla^2\rho(\mathbf{r}_c)$, i.e., $\mathrm{tr}(\mathbf{\Lambda}) = \partial^2\rho(\mathbf{r}_c)/\partial x_1^2 + \partial^2\rho(\mathbf{r}_c)/\partial x_2^2 + \partial^2\rho(\mathbf{r}_c)/\partial x_3^2 = \nabla^2\rho(\mathbf{r}_c)$. The eigenvalues of $\mathbf{\Lambda}$ are denoted $\lambda_i = \partial^2\rho(\mathbf{r}_c)/\partial x_i^2$ (Bader 1990). The first two eigenvalues, λ_1 and λ_2, (the curvatures

of $\rho(\mathbf{r}_c)$ measured perpendicular to the bond path) are associated with two orthogonal eigenvectors that are oriented perpendicular to the bond path and the third, λ_3, (the curvature of $\rho(\mathbf{r}_c)$ measured parallel to the bond path) is associated with a third eigenvector that is oriented perpendicular to the two orthogonal eigenvectors and parallel to the bond path. As the choice of λ_1 and λ_2 is arbitrary, by convention, the one with the smallest magnitude is defined to be λ_1. As the signs of λ_1 and λ_2 are both negative, they define the degree to which $\rho(\mathbf{r}_c)$ is locally concentrated perpendicular to the bond path and, as the sign of λ_3 is positive, it defines the degree to which $\rho(\mathbf{r}_c)$ is locally depleted along the bond path in the direction of the bonded atoms. If the magnitude of $\lambda_1 + \lambda_2$ is greater than λ_3, then $\nabla^2\rho(\mathbf{r}_c)$ is necessarily negative and $\rho(\mathbf{r}_c)$ is indicated to be locally concentrated at $\mathbf{r}_c$. If the converse is true and the magnitude of $\lambda_1 + \lambda_2$ is less than λ_3, then $\nabla^2\rho(\mathbf{r}_c)$ is positive and $\rho(\mathbf{r}_c)$ is indicated to be locally depleted at $\mathbf{r}_c$ (Bader 1990). However, when $\nabla^2\rho(\mathbf{r}_c)$ is positive, for example, and $\rho(\mathbf{r}_c)$ is locally depleted at $\mathbf{r}_c$, it does not necessarily follow that $\rho(\mathbf{r}_c)$ will decrease in value when $\nabla^2\rho(\mathbf{r}_c)$ actually increases in value (Gibbs et al. 1999a). Nonetheless, the magnitude and the sign of $\nabla^2\rho(\mathbf{r}_c)$ and the value of $\rho(\mathbf{r}_c)$ have been used to classify the character of a bond. As stressed by Bader and Essén (1984), a bond qualifies as a shared covalent interaction when $\nabla^2\rho(\mathbf{r}_c)$ is negative and large in magnitude and $\rho(\mathbf{r}_c)$ is relatively large. In contrast, when $\nabla^2\rho(\mathbf{r}_c)$ is positive and large in magnitude and $\rho(\mathbf{r}_c)$ is relatively small, the bond qualifies as a closed shell ionic interaction.

It is also well known that the value of $\rho(\mathbf{r}_c)$ provides a measure of the strength of a bond; the greater its value, the shorter the bond (Feynman 1939; Berlin 1951; Bader 1990). In cross-section, the electron density distribution of such a bond varies between being circular (isotropic) and elliptical (anisotropic) as revealed by its ellipticity, $\epsilon = (\lambda_1/\lambda_2 - 1)$. For a pure σ-bond like the single C-C bond in ethane, C_2H_6, the ϵ-value is zero, indicating that the bond electron density distribution at the bond critical point, bcp, is isotropic in cross section. However, for a bond with partial π-character like the C-C bond in benzene, $(CH)_6$, the electron density distribution extends more into space in the direction of the two π-orbitals than perpendicular to them, resulting in an anisotropic distribution and an ϵ-value of 0.23 (Bader 1990). Also, the magnitude of the ellipticity of a bond can be used as a measure of its stability. As observed by Bader (1990), a progressive decrease in $|\lambda_2|$ and its ultimate disappearance signifies that the magnitude of ϵ must increase dramatically as the bond path disappears and the bond is ultimately broken. Thus, bonds with unusually large ellipticity values are considered to be potentially unstable and to cleave when the bond path disappears.

The distance between a bonded atom and the critical point provides a measure of the size of the atom measured along the bond vector, referred to as its bonded radius. The bonded radius of an anion like the oxide anion, $r_b(O)$, has been found to increase regularly with increasing bond length and decreasing electronegativity of the cation to which it is bonded (Feth et al. 1993; Hill et al. 1997). As anions in earth materials are commonly bonded to more than one cation, they usually exhibit several bonded radii with a different one along each of the bond vectors to its coordinating cations. For example, the three-coordinate OC oxide anion in microcline, $KAlSi_3O_8$, is highly polarized with a bonded radius of 0.94 Å in the direction of the SiO bond vector, 1.00 Å in the direction of the AlO bond vector and 1.45 Å in the direction of the KO bond vector (G.V. Gibbs et al., in preparation).

Recently, bond critical point properties were derived for electron density distributions generated for a set of geometry-optimized model structures for the high-pressure silica polymorph coesite for pressures up to 15 Gpa, using first-principles calculations (G.V. Gibbs et al., submitted). The bond lengths and angles of the model structure match not only those observed for coesite at ambient conditions but also those observed for the compressed structure to within a few percent. As the SiOSi angles of the model structure increase from 136° to 180°, the SiO bond lengths, R(SiO), decrease regularly from 1.620 Å to 1.592 Å. For sake of comparison, the observed SiOSi angles increase from 137° to 180° as the observed SiO bond lengths decrease from 1.621 Å to 1.595 Å (Gibbs et al. 1977). With increasing angle and decreasing bond length, the value of $\rho(\mathbf{r}_c)$ at the bond critical points along the SiO bond paths of the model increases linearly (the coefficient of determination, $r^2 = 0.95$) from 0.959 to 1.002 eÅ^{-3} as the bonded radii of the oxide anions decrease linearly ($r^2 = 0.99$) from 0.951 to 0.930 Å. Concomitant with these small changes, the average curvature of $\rho(\mathbf{r}_c)$, $|\lambda_{1,2}| = 1/2(|\lambda_1 + \lambda_2|)$, measured perpendicular to the bond paths, increases linearly ($r^2 = 0.95$) from 6.16 to 6.68 eÅ^{-5} while λ_3, the curvature of $\rho(\mathbf{r}_c)$ measured parallel to the path, increases ($r^2 = 0.99$) from 34.83 to 38.81 eÅ^{-5}. With these changes, $\nabla^2\rho(\mathbf{r}_c)$ necessarily increases linearly ($r^2 = 0.997$) from 22.95 to 27.68 eÅ^{-5}. Despite the increase in $\nabla^2\rho(\mathbf{r}_c)$ and the progressive local depletion of $\rho(\mathbf{r}_c)$, the value of $\rho(\mathbf{r}_c)$ actually increases. In addition, the ellipticity of the SiO bonds in the model structure decreases to 0.0 as the SiOSi angle increases to 180°, a feature that has been ascribed to the engagement of two of the p-orbitals on the oxide anion in forming a weak π-bond with Si involving both orbitals when the SiOSi angle is straight (Gibbs et al. 1994). With decreasing SiO bond length and increasing SiOSi angle, the model structure calculations indicate that the electron density distribution along the bond paths increases slightly as its profile sharpens both parallel and perpendicular to the bond path. Concomitant with these changes, the bond critical point, $\mathbf{r}_c$, along the SiO bond paths shifts toward the oxide anion and the electron density distribution of the bond becomes circular in cross-section (G.V. Gibbs et al., in preparation).

In ground-breaking studies of the bond critical point properties for natural materials, Downs (1995) and

Downs and Swope (1992) completed structural analyses and generalized scattering factor (GSF) least-squares refinements of the electron density distribution, $\rho(\mathbf{r})$, for coesite and danburite, $CaB_2Si_2O_8$, respectively. Analyses of the topological properties of the electron density distributions revealed that the $\rho(\mathbf{r}_c)$ values for the SiO bonds range between 0.93 and 1.16 eÅ^{-3} a range of values that overlaps that derived for the model structure of coesite. A more recent determination of the bcp properties of the SiO bonds for the framework silicate, scolecite, $Ca[Al_2Si_3O_{10}]\cdot 3H_2O$, yielded a similar range of values (0.89–1.17 eÅ^{-3}, Kuntzinger et al. 1998). However, despite its longer bond lengths (1.637–1.647 Å) observed for topaz, $Al_2SiO_4F_2$, an analysis of the experimental electron density distribution of this orthosilicate displays somewhat larger $\rho(\mathbf{r}_c)$ values (1.18–1.36 eÅ^{-3}) (Ivanov et al. 1998) than observed, on average, for coesite, danburite, and scolecite (Downs 1995; Downs and Swope 1992; Kuntzinger et al. 1998).

As expected, the $\rho(\mathbf{r}_c)$ values observed for the SiO bonds are larger than those reported for the tetrahedral AlO bonds in scolecite (0.54–0.72 eÅ^{-3}) (Kuntzinger et al. 1998) and the octahedral AlO bonds in topaz (0.60–0.71 eÅ^{-3}) (Ivanov et al. 1998). In addition, the $\rho(\mathbf{r}_c)$ values observed for the AlO bonds are somewhat larger than those reported earlier for the shorter and more ionic BeO bonds in bromellite (~0.55 eÅ^{-3}; Downs 1991). Likewise, the $\rho(\mathbf{r}_c)$ values reported for the relatively long CaO bonds (2.40–2.61 Å) in both danburite and scolecite are relatively small (0.12–0.28 eÅ^{-3}) (Downs and Swope 1992; Kuntzinger et al. 1998).

Contrary to the trends given by the model calculations, the SiO bond lengths observed for both coesite and danburite are found to be independent of the observed values of $\rho(\mathbf{r}_c)$. In contrast, a very weak ($r^2 = 0.34$) but significant, negative correlation exists between the interatomic distance R(SiO) and the $\rho(\mathbf{r}_c)$ values observed for scolecite (Kuntzinger et al. 1998). In contrast, the SiO bond lengths observed for topaz are highly correlated ($r^2 = 0.95$) with R(SiO) decreasing slightly but systematically from 1.647 Å to 1.632 Å as $\rho(\mathbf{r}_c)$ increases from 1.18 to 1.36 eÅ^{-3}. Also, as reported for the model structure, the ellipticities of the SiO bonds in coesite are observed to decrease in value as the SiO-Si angle widens and the SiO bonds decrease in length (Gibbs et al. 1994).

While the tetrahedral AlO bond lengths in scolecite do not correlate with $\rho(\mathbf{r}_c)$ (Kuntzinger et al. 1998), the octahedral AlO bond lengths in topaz decrease regularly, ($r^2 = 0.88$) from 1.900 to 1.887 Å as $\rho(\mathbf{r}_c)$ increases from 0.60 to 0.71 eÅ^{-3} (Ivanov et al. 1998). Unlike the observed SiO bonds in coesite and danburite, as $\rho(\mathbf{r}_c)$ increases for the CaO bonds in danburite from 0.14 to 0.18 eÅ^{-3}, R(CaO) decreases linearly from 2.50 to 2.40 Å. In addition, the CaO bond lengths in scolecite are highly correlated with $\rho(\mathbf{r}_c)$ with an r^2 value of 0.95 (Kuntzinger et al. 1998). The lengths of the BO bonds in danburite also tend to decrease with increasing $\rho(\mathbf{r}_c)$, but the trend is not significant.

The average curvatures of $\rho(\mathbf{r}_c)$, $|\lambda_{1,2}|$ observed perpendicular to the SiO bond paths of danburite (6.8 eÅ^{-5}, coesite (7.0 eÅ^{-5}), and scolecite (6.6 eÅ^{-5}) are somewhat larger than that (6.4 eÅ^{-5}) derived for the model coesite structure (Downs and Swope 1992; Downs 1995; Kuntzinger et al. 1998). On the other hand, the curvatures recorded along the paths, λ_3, have a much larger value of ~34 eÅ^{-5}, somewhat smaller than that calculated (~36 eÅ^{-5}) for the coesite structure. Because of the smaller value of λ_3, $\nabla^2\rho(\mathbf{r}_c) = \lambda_1 + \lambda_2 + \lambda_3 = \sim 20$ eÅ^{-5} is smaller than that calculated for coesite (~23 eÅ^{-5}). The λ_3 values observed for coesite tend to increase with decreasing R(SiO), as indicated by the model calculations. Also, the SiO bond lengths in scolecite show a weak but significant correlation with both $\lambda_{1,2}$ and λ_3. In contrast, the $\rho(\mathbf{r}_c)$ values reported for the SiO bonds of topaz are substantially smaller, ranging between 8.2 eÅ^{-5} and 10.9 eÅ^{-5} (Ivanov et al. 1998). The values observed for $|\lambda_{1,2}|$ and $\rho(\mathbf{r}_c)$ for danburite and coesite are both independent of R(SiO). However, the $\rho(\mathbf{r}_c)$ values recorded for both scolecite and danburite show a weak but significant correlation with R(SiO) in the direction indicated by the model calculations.

The bonded radii of the oxide anions, r_b(O), measured along the SiO bond vectors in coesite, correlate ($r^2 = 0.93$) with R(SiO), the shorter the bond, the smaller the radius of the anion as observed in the model calculations (Gibbs et al. 1992). Also, the average radius of the anion in coesite, 0.95 Å is slightly larger than that (0.94 Å) obtained for the model structure. No correlation between R(SiO) and r_b(O) obtains for danburite. In the case of scolecite, R(SiO) is significantly correlated with r_b(O) with an r^2 value of 0.78 (Kuntzinger et al. 1998). The bonded radii of the oxide anions were not reported in the topaz study; nor were the curvatures of $\rho(\mathbf{r}_c)$ (Ivanov et al. 1998).

The bonded radii of the oxide anions measured along the BO vectors in danburite increase from 0.97 Å to 1.01 Å as R(BO) increases from 1.45 Å to 1.50 Å (Downs and Swope 1992). Likewise, the radii of the anions along the CaO bond vectors increase linearly from 1.18 Å to 1.24 Å as R(CaO) increases from 2.40 Å to 2.50 Å. In addition, r_b(O) is highly correlated with the observed CaO bond lengths for scolecite (Kuntzinger et al. 1998). On the whole, each of the oxide anions bonded to Si, B, and Ca in danburite is highly polarized, with r_b(O) ranging between ~0.95 Å to ~1.25 Å (Gibbs et al. 1992). As expected, the average $\rho(\mathbf{r}_c)$ value for the longer and more ionic CaO bonds in danburite is substantially smaller (0.15 eÅ^{-3}) than that observed for the SiO bonds while that of the BO bonds is marginally larger (1.05 eÅ^{-3}).

Experimental electron density distributions

In this study of aluminosilicate framework structures, experimental electron density distributions, static deformation $\Delta\rho(\mathbf{r}_c)$ maps and topological properties measured for the three isostructural fibrous zeolites (Waasmaier 1997), natrolite, $Na_2[Al_2Si_3O_{10}]\cdot 2H_2O$,

Table 1 Crystallographic data and room temperature data collections

	Natrolite[a]	Mesolite[b]	Scolecite[c]
Formula	$Na_2[Al_2Si_3O_{10}]\cdot 2H_2O$	$Na_2Ca_2[Al_2Si_3O_{10}]_3\cdot 8H_2O$	$Ca[Al_2Si_3O_{10}]\cdot 3H_2O$
Origin	Salesl, CSR	Poona, India	Pandulani, India
Dimensions	$0.16 \times 0.2 \times 0.3$ mm^3	$0.14 \times 0.16 \times 0.39$ mm^3	$0.22 \times 0.28 \times 0.5$ mm^3
Diffractometer	Enraf Nonius CAD4	Siemens P3	Enraf Nonius CAD4
Radiation	MoK_α	MoK_α	MoK_α
a (Å)	18.2929 (7)	18.4049 (8)	18.502 (1)
b (Å)	18.6407 (9)	56.655 (6)	18.974 (2)
c (Å)	6.5871 (6)	6.5443 (4)	6.525 (1)
β (°)	90	90	90.617 (7)
Vol. (Å^3)	2246.2	6823.9	2290.6
Space group	Fdd2	Fdd2	F1d1
Z	8	8	8
MW (g mol^{-1})	380.2	1164.9	392.3
D_x (g cm^{-3})	2.25	2.27	2.28
$F(000)$	1520	4688	1584
Scan mode	ω-scan	ω-2θ-scan	ω-scan
s_{max} (Å^{-1})	0.903	0.890	0.900
No. refl.	Full sphere 13920	Full sphere 40415	Full sphere 13656
I_{obs}	Lehman and Larsen (1974)	Lehman and Larsen (1974)	Lehman and Larsen (1974)
Abs. corr.	Gaussian, $8 \times 8 \times 8$ Coppens et al. (1965)	Gaussian, $8 \times 8 \times 8$ Coppens et al. (1965)	Gaussian, $14 \times 14 \times 10$ Coppens et al. (1965)
R_{int} (F^2)	0.008	0.0189	0.0140
Unique refl. $\lvert F\rvert > 3\sigma$	3471	8529	6902

[a] Stuckenschmidt et al. (1993)
[b] Stuckenschmidt and Kirfel (1999)
[c] Stuckenschmidt et al. (1997)

Table 2 Agreement results from IAM and GSF refinements

	IAM			GSF		
	Natrolite[a]	Mesolite[b]	Scolecite[c]	Natrolite	Mesolite	Scolecite
N_{refl}	3471	8529	3478	3462	8529	6902
N_{par}	86	318	170	422	1309	862
N_{refl}/N_{par}	40.36	26.82	20.46	8.20	6.51	8.00
$R(F)$	0.0112	0.022	0.012	0.0061	0.0165	0.0073
$wR(F)$	0.0170	0.019	0.014	0.0060	0.0197	0.0093
GoF	4.28	1.59	3.22	1.47	0.70	1.08

$$R(F) = \sum \| |F_0| - |F_c| \| / \sum |F_0|$$

$$wR(F) = \left[\sum w(|F_0| - |F_c|)^2 / \sum w|F_0|^2 \right]^{1/2}$$

$$\mathrm{GoF} = \left[\sum w(|F_0| - |F_c|)^2 / (N_{refl} - N_{par}) \right]^{1/2}$$

[a] Stuckenschmidt et al. (1997), Friedel pairs averaged
[b] Stuckenschmidt et al. (1993)
[c] Stuckenschmidt and Kirfel (1999)

mesolite, $Na_2Ca_2[Al_2Si_3O_{10}]\cdot 8H_2O$, and scolecite are described and compared with those determined for coesite, danburite, and topaz. The electron density distribution for natrolite was previously reported by Ghermani et al. (1996). The properties of scolecite will be compared with those recently published by Kuntzinger et al. (1998). Another goal, as we have already seen, will be to explore whether the trends in the bcp properties for the SiO bonds are in the same direction as those derived for coesite and a variety of hydroxyacid molecules (Hill et al. 1997). Another will be to explore whether similar trends hold for the more ionic AlO, CaO, and NaO bonds in the zeolites.

The crystal structure of each of the three zeolites consists of an ordered framework of $Al_2Si_3O_{10}$ composition of corner sharing SiO_4 and AlO_4 tetrahedral oxyanions. The large voids in the framework are occupied by H_2O molecules together with Na^+ in natrolite, Ca^{+2} in scolecite, and Na^+ and Ca^{+2} in mesolite. In conformity with the constraints imposed on the structures of the zeolites by their observed space group types, natrolite contains 6 nonequivalent SiO bonds and 4 nonequivalent AlO bonds, mesolite contains 18 SiO bonds and 12 AlO bonds, and scolecite contains 12 SiO bonds and 8 AlO bonds for a total of 36 nonequivalent SiO bonds and 24 AlO bonds. This large number of bonds, together with their bcp properties, provides a relatively large data set which can be used to test whether the trends predicted by theory hold and are statistically meaningful for the experimental data set.

Data collections and structure refinements

Crystals of natrolite, scolecite, and mesolite were investigated by single-crystal X-ray diffractometry using MoKα radiation. Prior to

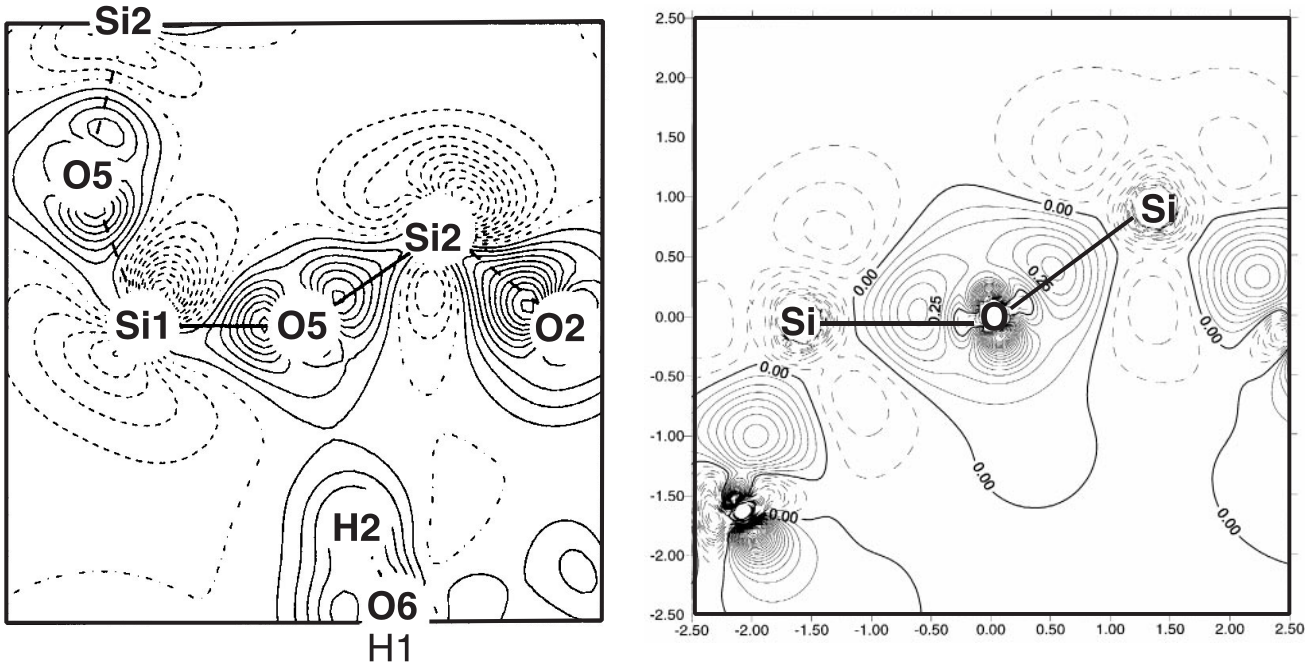

Fig. 1 *Left* static deformation electron density distribution $\Delta\rho(\mathbf{r})$ map generated through a selected SiOSi plane in natrolite, contour interval at 0.05 eÅ^{-3}. *Right* theoretical $\Delta\rho(\mathbf{r})$ map through the SiOSi plane of a geometry optimized $H_6Si_2O_7$ molecule, generated with wave functions obtained at the Becke3LYP/6-311G(2d,p) level, contour levels at 0.05 eÅ^{-3}. Positive contour lines are *continuous*, the negative are *dashed* and the zero line is *dot-dashed*

the mesolite diffraction experiment, the crystal material was studied by microprobe analyses, yielding homogeneous samples of compositions (Waasmaier 1997):

Natrolite: $Na_{1.97(1)}[Al_{2.00(1)}Si_{3.01(1)}O_{10}]\cdot 2H_2O$,

Scolecite: $Ca_{1.01(1)}[Al_{2.01(1)}Si_{2.99(1)}O_{10}]\cdot 3H_2O$,

Mesolite: $Na_{1.99(3)}Ca_{2.04(1)}[Al_{6.00(4)}Si_{8.98(3)}O_{30}]\cdot 8H_2O$.

With permission of the authors, data for natrolite and scolecite were taken from earlier measurements of Stuckenschmidt et al. (1993, 1997), respectively. These data were complemented by additional measurements on mesolite (Waasmaier 1997; Stuckenschmidt and Kirfel 1999). The conventional structure analyses for natrolite and scolecite were reported earlier and Table 1 gives a complete summary of the crystallographic data and interesting details of the data collections and processings for comparison. The somewhat poorer quality of the mesolite data is attributed to the large magnitude of the tripled *b* cell edge giving rise to some problems with reflection overlap.

In order to obtain really comparable results, the new GSF structure refinements were carried out using the same strategy and the program package VALRAY96 (Stewart and Spackman 1983; Stewart et al. 1996) which includes the option for topological analysis of the refined total model electron density distribution. All refinements (Waasmaier 1997; Waasmaier et al. 1997) were based on:

- Structure amplitudes $|F|$.
- Reflection weights $w = [\sigma(F)]^{-2}$, where $\sigma(F)$ is calculated from both counting statistics and internal agreement R_{int} of the data set.
- Reflections with $|F| \geq 3\sigma$ and assigning zero weights to reflections with $w\Delta F \geq 3$.
- Isotropic type 1 extinction corrections, Lorentzian distribution (largest intensity corrections were less than 10% in each refinement).
- Neutral atoms using localized wave functions (Stewart and Spackman 1983; Clementi 1965).
- Anomalous dispersion corrections taken from Sasaki (1989).
- Assigning to all nonhydrogen atoms three monopole functions with populations PCR = Z, PSH, and PVL (for hydrogens PCR = 0, PSH = 1).
- Multipoles up to hexadecapoles for the "heavy" atoms, whereas hydrogen deformations were restricted to quadrupoles.
- Individual radial expansion coefficients $\alpha_{l,p}$ for each atom and multipole order.
- "Block mode" due to the large numbers of variables, i.e., different types of variables like crystallographic standard parameters or multipole populations were refined in subsequent cycles, prior to a final full matrix cycle.
- First derivatives for the normal equations (test calculations including second derivatives failed to yield significant parameter changes in the case of natrolite and became too time-consuming for the two other structures).

Finally for natrolite and scolecite, the hydrogen atoms were fixed at the positions obtained in single-crystal neutron diffraction experiments (Artioli et al. 1984; Joswig et al. 1984), whereas for mesolite, the hydrogen coordinates were included into the list of variables, since neutron data are not available.

Starting with the independent atom (IAM) refinements and successively introducing deformation parameters the refinements converged at the *R*-values given in Table 2. The comparison of the conventional IAM refinement results (Stuckenschmidt et al. 1993, 1997) with those finally obtained from the GSF refinements indicates significant model improvements according to the *R*-factor tests (Hamilton 1965).

Deformation electron density distributions

Generalized structure factor, GSF, models of the electron density distributions for the three zeolites were generated in direct space lattice summations over the pseudoatoms of the three structures. Static deformation maps, $\Delta\rho(\mathbf{r})_{\text{stat}}$, were obtained using only the multipole functions in the direct space calculations. The respective model qualities were assessed by means of residual maps, $\Delta\rho(\mathbf{r})_{\text{res}}$, calculated by Fourier summations up to $s_{\max} = 0.70$ Å^{-1}. These maps exhibited maximum residual features of at most 0.1 eÅ^{-3} for both natrolite and scolecite and of up to 0.15 eÅ^{-3} for mesolite. These findings conform with the estimated mean errors of the

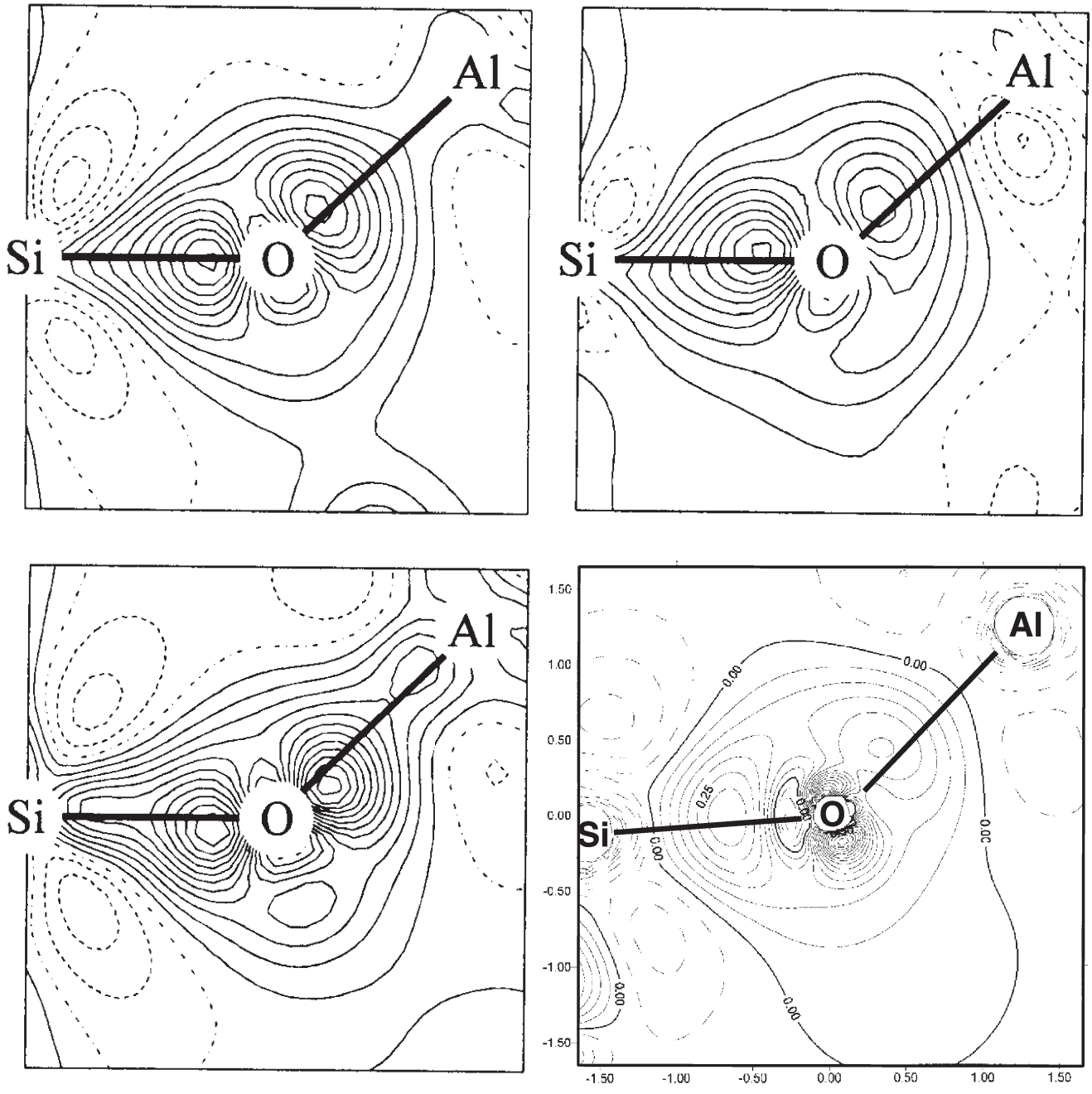

Fig. 2 "Chemical average" static $\Delta\rho(\mathbf{r})$ distribution through the SiOAl angles of natrolite (*top left*), scolecite (*top right*), and mesolite (*bottom left*). For comparison, a theoretical $\Delta\rho(\mathbf{r})$ map generated with wave functions obtained at the Becke3LYP/6-311G(2d,p) level through the SiOAl plane of the $H_6SiAlO_7^{-1}$ molecule is displayed at the bottom right. See legend to Fig. 1 for details of contours

electron density distribution (Cruickshank 1949) of 0.01, 0.037, and 0.054 eÅ^{-3} for natrolite, scolecite, and mesolite, respectively.

Figure 1 compares a $\Delta\rho(\mathbf{r})_{stat}$ map observed for the Si1O5Si2 bridging angle in natrolite with that calculated through the SiOSi dimer of a geometry optimized $H_6Si_2O_7$ molecule (C_v point symmetry). The theoretical map shows a peak of deformation electron density along each of the SiO bonds located ~0.6 Å from the oxide anion, whereas the corresponding peaks in the experimental map are closer at ~0.4 Å from the anion. The maps differ in that the peaks recorded for natrolite are somewhat higher and more polarized towards Si and the peak in the lone pair region of the oxide anion displayed in the theoretical map is missing. Not only is this peak missing in the maps published earlier for scolecite (Kuntzinger et al. 1998), but two peaks rather than one well-defined peak are displayed along the SiO bonds in these earlier maps, one in the vicinity of the valence shell of the oxide anion and the other in the vicinity of the valence shell of the Si atom. Of the two peaks, the one at 0.45 Å from the oxide anion is substantially higher (0.60–0.70 eÅ^{-3}) than that (0.2–0.3 eÅ^{-3}) at ~0.65Å from Si. On the other hand, static deformation maps obtained in the multipole analysis of the electron density distribution reported for topaz display single, well-defined peaks along each of the SiO bonds of the silicate tetrahedron, ranging in height between 0.5 and 0.6 eÅ^{-3}.

By calculating for each structure the average of chemically corresponding deformation density distributions, "chemically averaged" deformation maps of the SiOAl angles for natrolite,

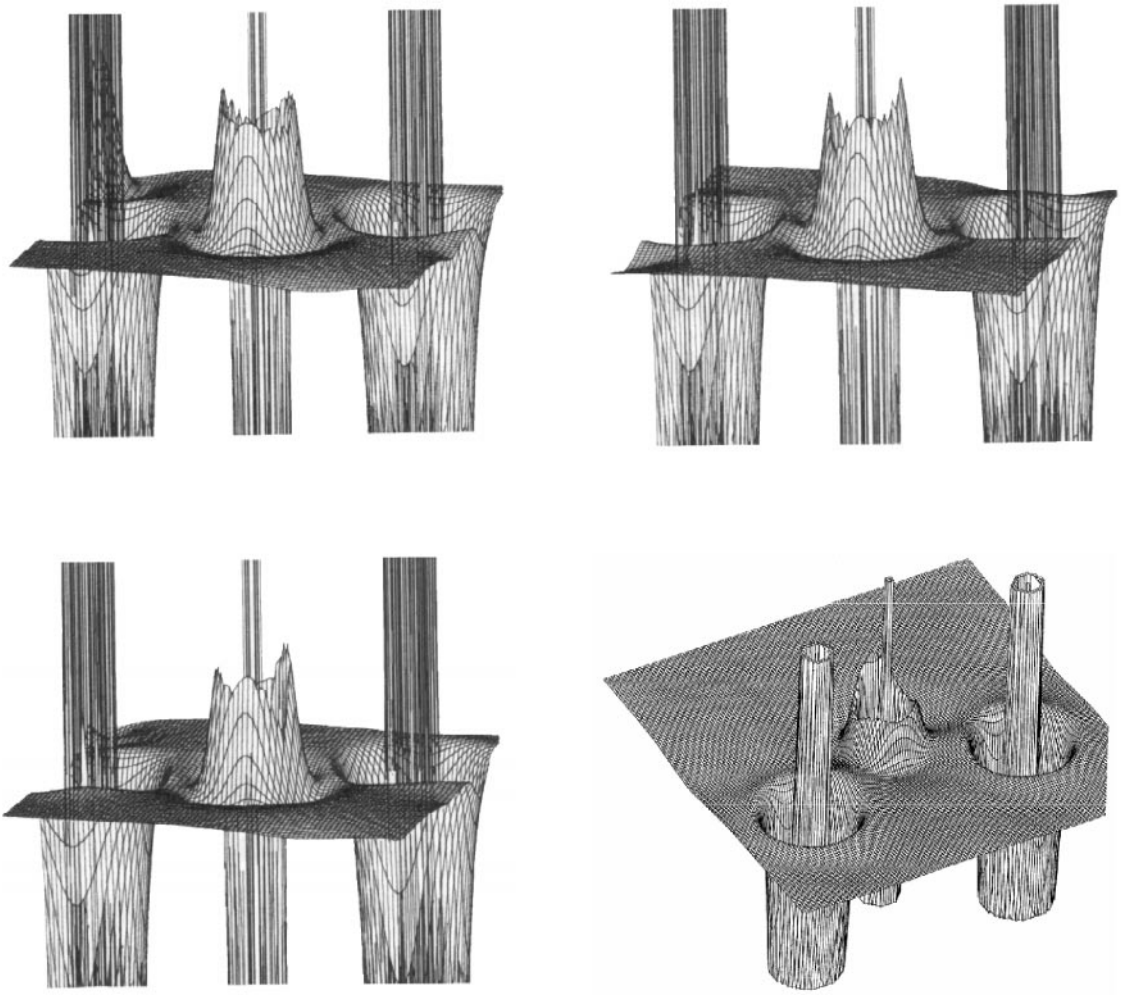

Fig. 3 Relief maps of $-\nabla^2\rho(\mathbf{r})$ generated for the Si1O5Si2 plane of natrolite (*top left*), scolecite (*top right*), and mesolite (*bottom left*). For comparison, a $-\nabla^2\rho(\mathbf{r})$ map calculated through the SiOSi plane of a $H_6Si_2O_7$ molecule is displayed at the *bottom right*. See legend to Fig. 1 for details of the MO calculations

scolecite and mesolite were obtained (Fig. 2a–c). As expected from electronegativity considerations and the longer AlO bond length, the peaks along the SiO bonds are higher ($\sim$0.55 eÅ^{-3}), on average, than those along the AlO bonds ($\sim$0.45 eÅ^{-3}) as observed earlier for scolecite (Kuntzinger et al. 1998). As displayed in Fig. 1, the peaks along the SiO bonds are polarized in the direction of the Si cation. Likewise, the peak along the AlO bond in mesolite is polarized towards the Al cation. In contrast, the peaks along the bond in the other two zeolites show little or no polarization. All three maps show a small peak in the lone pair region of the oxide anion. For purposes of comparison, a $\Delta\rho(\mathbf{r})$ map was calculated for the SiOAl dimer of the H_6SiAlO^{1-} molecule (Fig. 2d). As observed, the peak height along the AlO bond is less than that along the SiO bond. Like the peaks in the plane of the SiOSi angle of the $H_6Si_2O_7$ molecule, those displayed by the map of the SiOAl angle are substantially lower in height than those observed, on average, for the three zeolites. As observed for the zeolites, the theoretical map displays a peak on the exterior side of the SiOAl angle.

The topographies of the deformation maps, generated for the SiOAl angles in the Kuntzinger et al. (1998) study, are similar to those displayed for the SiOSi angles with two peaks situated along the SiO and the AlO bonds with the larger of the two localized in the vicinity of the oxide anion. As observed for the three zeolites, the peaks along the AlO bond are smaller than those along the SiO bonds; also several of the maps display a peak in the lone pair region of the oxide anion. Again, the Al, Si, and O atoms are each surrounded by several peaks in the vicinities of their valence shells.

Bond critical point properties of SiO bonds

In furthering our understanding of the observed electron density distributions, topological analyses of the total GSF model distributions for the zeolites were completed together with an analytical evaluation of the gradient and the Laplacian distributions and a calculation of their bcp properties (Bader 1990). Relief $-\nabla^2\rho(\mathbf{r}_c)$ maps of the GSF distributions comprising the Si1O5Si2 angles in natrolite, scolecite and mesolite are depicted in Fig. 3. As displayed by the relief map calculated for the $H_6Si_2O_7$ molecule (Fig. 3d) and observed for danburite, coesite, and topaz, the valence shell charge concentration, VSCC, of each oxide anion is well developed while that of the Si cation is much more diffuse and poorly developed, and even absent in some cases (Downs and Swope 1992; Downs 1995; Ivanov et al. 1998). In addition, as observed for the molecule, small peaks exist in the VSCC of the oxide anions in the vicinity where the shell of the anion crosses the two bond paths (Gibbs et al. 1999b). However, unlike the molecule, maxima are missing, for the most part, in the lone pair regions of the oxide anions for the zeolites. As reported by Gibbs et al. (1999b) for the $H_6Si_2O_7$ molecule, the small maxima in the VSCC of the oxide anion in the vicinity of the SiO bond vectors can be ascribed to bonded electron pairs. They were found to lie in the plane of the SiOSi angle at a distance of $\sim$0.4 Å from the oxide anion and are displaced off the SiO bond vectors toward the interior angle by $\sim$18°. The single

Table 3 Bond lengths, bcp properties, and cation electronegativities of the SiO bonds in natrolite

Bond	R(SiO)	r_b(O)	$\rho(\mathbf{r}_c)$	$\lambda_{1,2}$	λ_3	$\nabla^2\rho(\mathbf{r}_c)$	χ_M
Si1-O1	1.6072 (2)	0.916	0.93	−8.44	28.26	14.53	1.806
Si1-O5	1.6296 (2)	0.946	0.93	−6.68	27.88	14.53	1.793
Si2-O3	1.6120 (2)	0.937	1.09	−8.76	32.22	14.70	1.864
Si2-O4	1.6137 (2)	0.936	1.10	−8.83	31.72	14.05	1.869
Si2-O2	1.6201 (1)	0.943	1.11	−8.89	31.76	13.98	1.873
Si2-O5	1.6373 (2)	0.947	0.96	−7.28	27.49	12.94	1.807
	⟨1.6195⟩	⟨0.938⟩	⟨1.018⟩	⟨−8.15⟩	⟨29.98⟩	⟨14.12⟩	⟨1.835⟩

Table 4 Bond length, bcp properties, and cation electronegativities of the SiO bonds in mesolite

Bond	R(SiO)	r_b(O)	$\rho(\mathbf{r}_c)$	$\lambda_{1,2}$	λ_3	$\nabla^2\rho(\mathbf{r}_c)$	χ_M
Si1-O1	1.6075 (6)	0.920	1.16	−9.46	30.13	11.21	1.899
Si1-O5	1.6326 (6)	0.956	0.85	−6.51	21.83	8.80	1.754
Si10-O10	1.6014 (7)	0.919	1.15	−8.34	32.29	15.60	1.895
Si10-O100	1.6142 (6)	0.916	1.13	−8.62	26.69	9.46	1.892
Si10-O500	1.6147 (6)	0.972	0.86	−6.06	25.16	13.05	1.753
Si10-O50	1.6445 (6)	0.977	0.81	−6.29	26.47	13.89	1.724
Si2-O3	1.6064 (7)	0.931	0.99	−6.86	30.51	16.78	1.828
Si2-O2	1.6123 (5)	0.937	1.16	−9.35	28.25	9.54	1.894
Si2-O4	1.6294 (6)	0.954	1.10	−9.03	30.36	12.30	1.863
Si2-O5	1.6356 (8)	0.934	1.00	−6.54	24.60	11.51	1.830
Si20-O40	1.5980 (6)	0.887	1.36	−11.95	24.90	10.00	1.989
Si20-O20	1.6146 (5)	0.952	1.07	−9.62	30.01	10.77	1.851
Si20-O300	1.6354 (7)	0.956	0.96	−7.18	24.82	10.47	1.803
Si20-O50	1.6464 (7)	0.959	0.94	−6.33	26.66	14.00	1.793
Si200-O30	1.6142 (7)	0.916	1.19	−9.84	24.84	5.17	1.914
Si200-O400	1.6153 (6)	0.956	1.00	−8.49	31.53	14.54	1.822
Si200-O200	1.6180 (5)	0.917	1.22	−9.71	25.26	5.83	1.926
Si200-O500	1.6339 (7)	0.942	1.04	−8.03	27.15	5.70	1.843
	⟨1.6207⟩	⟨0.939⟩	⟨1.053⟩	⟨−8.23⟩	⟨27.00⟩	⟨10.48⟩	⟨1.848⟩

Table 5 Bond lengths, bcp properties, and cation electronegativities of the SiO bonds in scolecite

Bond	R(SiO)	r_b(O)	$\rho(\mathbf{r}_c)$	$\lambda_{1,2}$	λ_3	$\nabla^2\rho(\mathbf{r}_c)$	χ_M
Si1-O10	1.5992 (2)	0.919	1.26	−9.75	28.05	8.55	1.938
Si1-O1	1.6116 (2)	0.916	1.20	−8.02	24.56	8.52	1.918
Si1-O5	1.6183 (2)	0.933	1.17	−9.22	25.42	6.99	1.898
Si1-O50	1.6417 (2)	0.980	1.00	−8.43	30.85	14.00	1.787
Si2-O30	1.6055 (2)	0.942	0.95	−6.20	33.71	21.23	1.806
Si2-O2	1.6126 (2)	0.905	1.30	−8.66	24.33	7.15	1.958
Si2-O5	1.6311 (3)	0.911	0.75	−3.88	30.13	22.37	1.723
Si2-O4	1.6341 (2)	0.945	1.22	−9.94	28.86	6.99	1.911
Si20-O40	1.5991 (2)	0.927	1.06	−5.84	28.13	16.45	1.857
Si20-O20	1.6094 (2)	0.957	1.10	−8.37	34.92	18.23	1.860
Si20-O3	1.6305 (2)	0.959	1.07	−7.49	28.58	13.60	1.846
Si20-O50	1.6442 (2)	0.973	1.01	−5.84	19.91	8.23	1.816
	⟨1.6198⟩	⟨0.939⟩	⟨1.090⟩	⟨−7.64⟩	⟨27.95⟩	⟨12.69⟩	⟨1.860⟩

small maximum in the lone pair region of the molecule has been ascribed to a lone pair local concentration of electron density in the plane of SiOSi angle at a distance 0.35 Å from the bridging oxide anion external to the SiOSi angle (Gibbs et al. 1999b). In all likelihood, it corresponds to the nonbonding peak in the deformation density on the external side of the apex of the SiOSi angle.

The observed SiO bond lengths and the bcp properties for the SiO bonds of natrolite, mesolite and scolecite are given in Tables 3–5, respectively. The SiO bond lengths show a relatively wide scatter when plotted against $\rho(\mathbf{r}_c)$ (Fig. 4a), but a linear regression analysis of the data set indicates that R(SiO) and $\rho(\mathbf{r}_c)$ are weakly correlated at the 3.5σ level with a negative slope [−0.053(15)] (the esd of the slope is given in parentheses). On the basis of the esd of the slope, it can be concluded that the negative trend between R (SiO) and $\rho(\mathbf{r}_c)$ is statistically significant and that the shorter bonds in the zeolites tend to have larger $\rho(\mathbf{r}_c)$ values, as reported above for the scolecite and topaz data and as indicated by the model calculations. The average $\rho(\mathbf{r}_c)$ value (1.05 eÅ^{-3}) for the three zeolites is in exact agreement with that observed for coesite (Downs 1995) and a few percent larger than that calculated for the coesite model (0.97 eÅ^{-3}). As observed for coesite, danburite, and scolecite, the bonded radii of the oxide anions in the zeolites tend to increase with increasing SiO bond length (Fig. 4b); the slope of the regression line is 0.42 (8). The average value (0.939 Å) of the radius is in close agreement with that observed for coesite (0.934 Å) and that calculated for the coesite model (0.944 Å). As predicted by the model calculations, the slope of the trend [0.004(1)] between $|\lambda_{1,2}|$ and R(SiO) is positive (Fig. 4c); the esd of the slope indicates that the trend is significant. The average value of $|\lambda_{1,2}|$ (8.0 eÅ^{-5}) for the zeolites is larger than that observed for coesite (7.0 eÅ^{-5}). The correlation between R(SiO) and λ_3 is negative [−0.0015(6)] as predicted by the model structure, but the trend is marginally signifi-

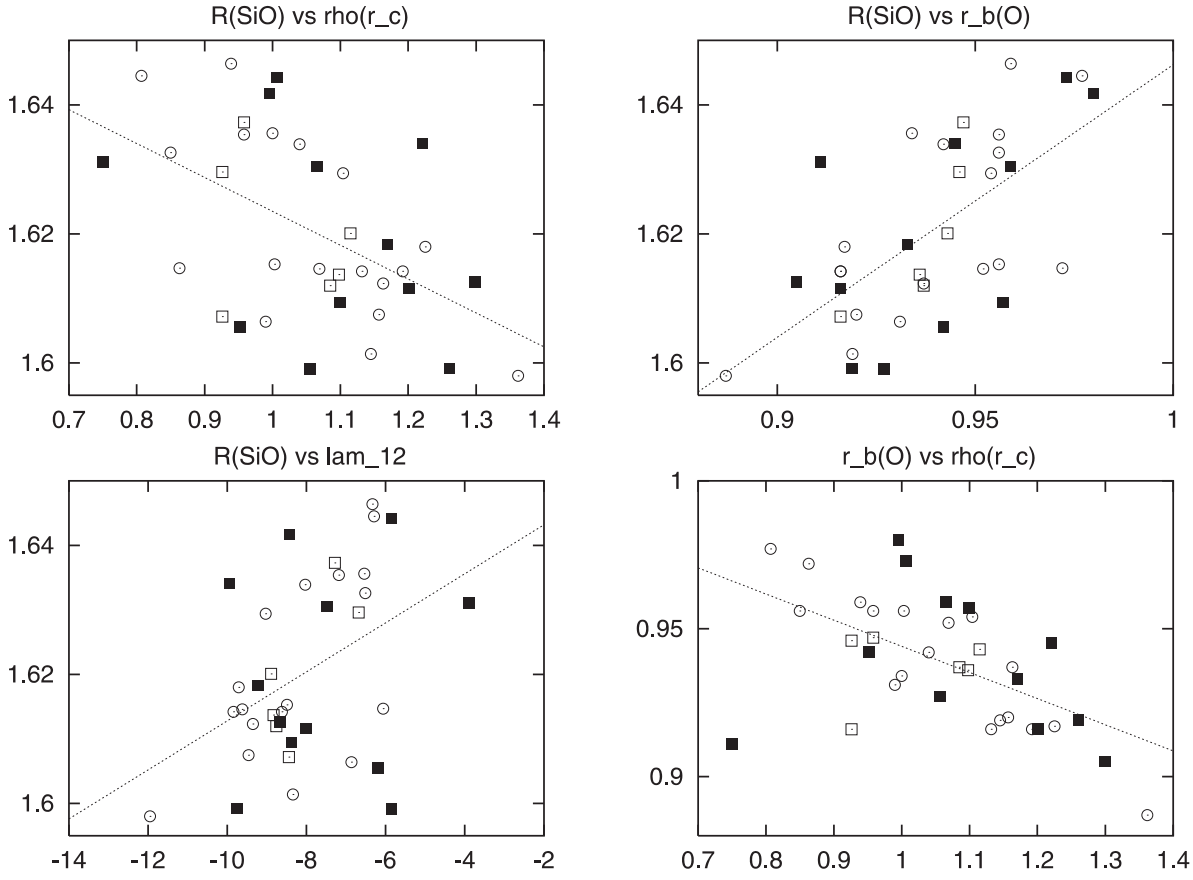

Fig. 4a–d Bond lengths and bcp properties of the SiO bonds in natrolite (*squares*), mesolite (*circles*), and scolecite (*full squares*). **a** R(SiO) vs. $\rho(\mathbf{r}_c)$ (*top left*). **b** R(SiO) vs. r_b(O) (*top right*). **c** R(SiO) vs. $\lambda_{1,2}$ (*bottom left*). **d** r_b(O) vs. $\rho(\mathbf{r}_c)$ (*bottom right*)

cant. In light of the marginally significant correlations between R(SiO) and the curvatures of $\rho(\mathbf{r}_c)$, it is not surprising that the regression analysis indicates that the value of $\nabla^2\rho(\mathbf{r}_c)$ is independent of R(SiO). The average λ_3 (28.3 eÅ^{-6}) and $\nabla^2\rho(\mathbf{r}_c)$ (12.4 eÅ^{-5}) values are likewise smaller than those observed for coesite (34.4 eÅ^{-5}, 20.3 eÅ^{-5}, respectively). In addition, given the correlations between R(SiO), $\rho(\mathbf{r}_c)$, and r_b(O), the negative correlation between $\rho(\mathbf{r}_c)$ and r_b(O) is expected (Fig. 4d). However, that between $\rho(\mathbf{r}_c)$ and $\nabla^2\rho(\mathbf{r}_c)$ is at variance with that predicted by the model structure for coesite. As the SiOSi and SiOAl angles in both natrolite and mesolite increase, the mean ellipticities of the bonds reaching the bridging oxide anions tend to decrease, as found in the model calculations; no such trend obtains for scolecite.

Bond critical point properties of the AlO bonds

The bcp properties calculated for the bonds of the AlO_4 tetrahedral oxyanions of the hydroxy aluminate molecules $H_9Al_3O_9$, H_6AlPO_7, and H_7AlSiO_7 exhibit the same sorts of trends with R(AlO) as found for the SiO bonds in the model coesite structure. They differ, however, in that average values of $\rho(\mathbf{r}_c) = 0.55$ eÅ^{-3} and $\lambda_{1,2} = \sim -3.5$ eÅ^{-5}, $\lambda_3 = \sim 25.0$ eÅ^{-5} and $\nabla^2\rho(\mathbf{r}_c) = \sim 17.9$ eÅ^{-5} for the AlO bonds are each smaller (see also Hill et al. 1997). The lengths and the bcp properties observed for the AlO bonds of the zeolites are given in Tables 6–8. The average bonded radius of the oxide anion (1.02 Å) is in exact agreement with that calculated for the molecules. However, unlike the bcp properties observed for the SiO bonds and as found for scolecite, none of the bcp properties for the AlO bonds correlates with R(AlO). However, the $\rho(\mathbf{r}_c)$ values for the AlO bonds correlate linearly with r_b(O), [−0.13(2)], λ_3, [−13(4)], and $\nabla^2\rho(\mathbf{r}_c)$, [−33(4)] (Fig. 5a–c, respectively). A negative correlation is obtained between r_b(O) and $\rho(\mathbf{r}_c)$ for the three hydroxy aluminate molecules as observed for the zeolites, but positive rather than negative correlations obtain between $\rho(\mathbf{r}_c)$ and both λ_3 and $\nabla^2\rho(\mathbf{r}_c)$.

Bond critical point properties of the NaO and CaO bonds

As obtained for the SiO and AlO bonds, the bcp properties of the NaO and CaO bonds were calculated (Tables 9, 10) and inspected for trends. The correlation between R(NaO) and $\rho(\mathbf{r}_c)$ is weak and marginally significant, whereas that between R(CaO) and $\rho(\mathbf{r}_c)$ (Fig. 6a) is highly significant, with both bonds decreasing in length as $\rho(\mathbf{r}_c)$ increases in value. On the other hand, both bond lengths are highly correlated with the bonded radius of the oxide anion;

Table 6 Bond length, bcp properties, and cation electronegativities of the AlO bonds in natrolite

Bond	R(AlO)	r_b(O)	$\rho(\mathbf{r}_c)$ 0.71	$\lambda_{1,2}$	λ_3	$\nabla^2\rho(\mathbf{r}_c)$	χ_M
Al-O3	1.7371 (2)	0.988	0.69	−4.66	23.71	14.00	1.554
Al-O1	1.7395 (2)	1.014	0.51	−3.95	19.42	19.41	1.442
Al-O4	1.7447 (2)	0.992	0.71	−4.97	22.51	12.57	1.564
Al-O2	1.7478 (1)	0.999	0.71	−5.23	23.74	13.27	1.561
	⟨1.7423⟩	⟨0.998⟩	⟨0.658⟩	⟨−4.70⟩	⟨22.30⟩	⟨14.81⟩	⟨1.530⟩

Table 7 Bond lengths, bcp properties, and cation electronegativities of the AlO bonds in mesolite

Bond	R(AlO)	r_b(O)	$\rho(\mathbf{r}_c)$	$\lambda_{1,2}$	λ_3	$\nabla^2\rho(\mathbf{r}_c)$	χ_M
Al1-O3	1.7299 (6)	0.987	0.84	−7.87	25.13	9.38	1.626
Al1-O200	1.7342 (5)	0.995	0.70	−5.31	22.75	12.12	1.553
Al1-O1	1.7359 (7)	1.003	0.66	−4.89	21.62	11.84	1.531
Al1-O4	1.7647 (6)	1.016	0.72	−5.61	22.35	11.13	1.558
Al10-O10	1.7370 (8)	1.011	0.60	−3.89	22.99	15.17	1.496
Al10-O30	1.7377 (6)	0.974	0.75	−6.16	17.84	5.52	1.587
Al10-O40	1.7379 (7)	0.998	0.67	−5.08	25.08	14.92	1.540
Al10-O20	1.7400 (6)	0.997	0.63	−4.40	22.21	13.41	1.516
Al100-O2	1.7470 (6)	1.005	0.69	−5.36	21.94	11.22	1.545
Al100-O400	1.7480 (6)	1.012	0.65	−4.53	23.85	14.80	1.523
Al100-O100	1.7484 (7)	0.997	0.71	−5.26	17.44	6.92	1.559
Al100-O300	1.7563 (6)	0.988	0.91	−7.71	18.12	2.70	1.655
	⟨1.7431⟩	⟨0.999⟩	⟨0.710⟩	⟨−5.50⟩	⟨21.78⟩	⟨10.76⟩	⟨1.557⟩

Table 8 Bond lengths, bcp properties, and cation electronegativities of the AlO bonds in scolecite

Bond	R(AlO)	r_b(O)	$\rho(\mathbf{r}_c)$	$\lambda_{1,2}$	λ_3	$\nabla^2\rho(\mathbf{r}_c)$	χ_M
Al1-O2	1.7375 (2)	0.995	0.74	−5.37	22.12	11.39	1.577
Al1-O1	1.7419 (2)	1.042	0.60	−3.78	19.92	12.35	1.484
Al1-O3	1.7525 (2)	1.017	0.70	−4.43	18.33	9.46	1.549
Al1-O4	1.7653 (2)	0.977	0.87	−5.23	15.63	5.17	1.644
Al10-O30	1.7402 (2)	0.968	0.84	−5.21	17.40	6.98	1.633
Al10-O20	1.7433 (2)	0.999	0.74	−3.69	20.90	13.53	1.572
Al10-O10	1.7442 (3)	1.049	0.45	−2.92	24.58	18.75	1.390
Al10-O40	1.7459 (3)	1.030	0.42	−2.98	26.78	20.81	1.369
	⟨1.7463⟩	⟨1.010⟩	⟨0.670⟩	⟨−4.20⟩	⟨20.71⟩	⟨12.31⟩	⟨1.527⟩

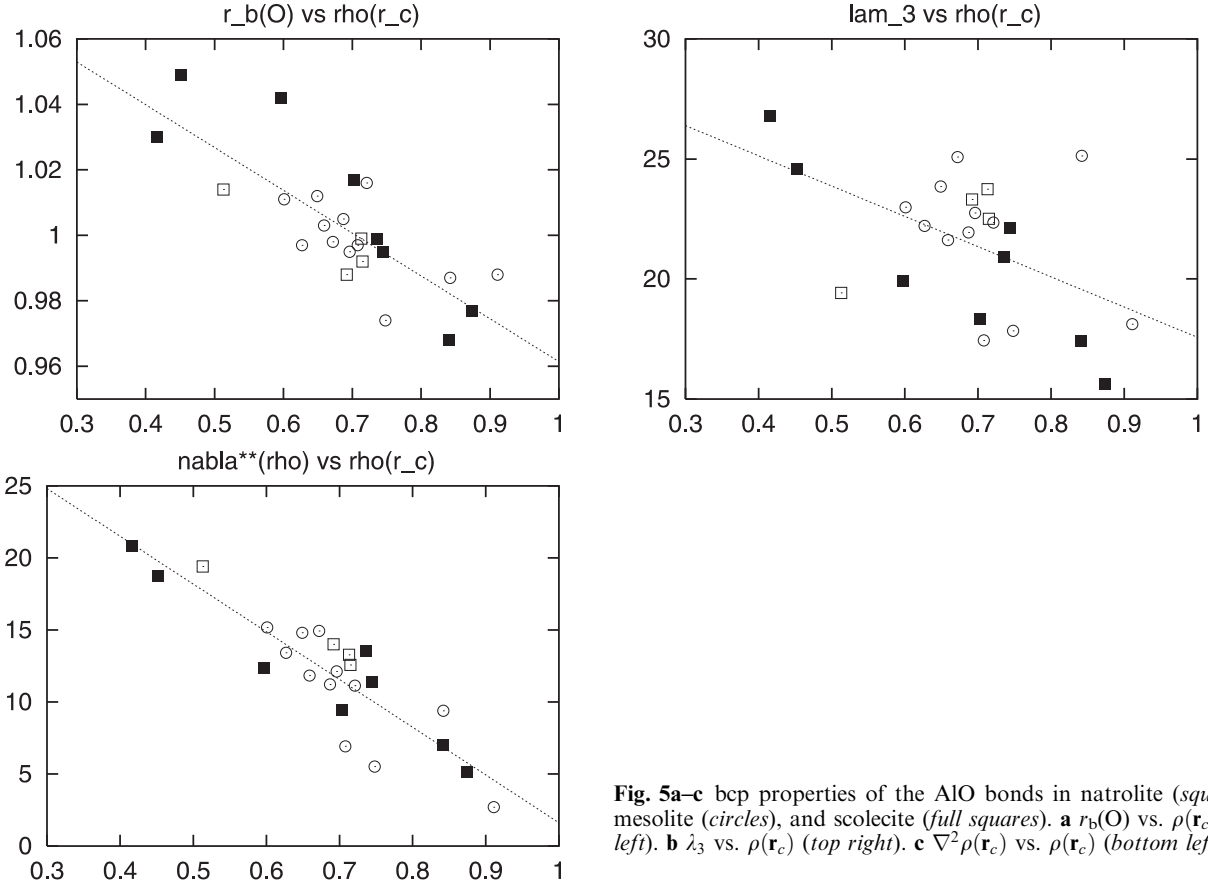

Fig. 5a–c bcp properties of the AlO bonds in natrolite (*squares*), mesolite (*circles*), and scolecite (*full squares*). **a** r_b(O) vs. $\rho(\mathbf{r}_c)$ (*top left*). **b** λ_3 vs. $\rho(\mathbf{r}_c)$ (*top right*). **c** $\nabla^2\rho(\mathbf{r}_c)$ vs. $\rho(\mathbf{r}_c)$ (*bottom left*)

Table 9 Bond lengths and bcp properties of the NaO bonds in natrolite (*top*) and mesolite (*bottom*)

Bond	R(NaO)	r_b(O)	$\rho(\mathbf{r}_c)$	$\lambda_{1,2}$	λ_3	$\nabla^2\rho(\mathbf{r}_c)$
Na-O3	2.3670(2)	1.322	0.12	−0.45	3.87	2.97
Na-O6	2.3702(3)	1.314	0.12	−0.58	3.50	2.34
Na-O6	2.3881(2)	1.340	0.11	−0.51	3.44	2.42
Na-O4	2.3952(2)	1.351	0.11	−0.29	3.46	2.88
Na-O2	2.5162(2)	1.434	0.08	−0.18	2.31	1.96
Na-O2	2.6162(2)	1.447	0.09	−0.27	1.77	1.24
Na-O6	2.3379(9)	1.264	0.19	−1.21	4.48	2.05
Na-O6	2.3425(7)	1.293	0.13	−0.67	4.06	2.73
Na-O400	2.3952(7)	1.389	0.12	−0.53	2.98	1.92
Na-O3	2.4050(6)	1.349	0.10	−0.22	2.73	2.29
Na-O2	2.5684(7)	1.451	0.11	−0.36	1.87	1.15
Na-O2	2.7344(7)	1.533	0.08	−0.22	1.24	0.80
	⟨2.4530⟩	⟨1.374⟩	⟨0.114⟩	⟨−0.46⟩	⟨2.98⟩	⟨2.06⟩

Table 10 Bond lengths and bcp properties of the CaO bonds in scolecite (*top*) and mesolite (*bottom*)

Bond	R(CaO)	r_b(O)	$\rho(\mathbf{r}_c)$	$\lambda_{1,2}$	λ_3	$\nabla^2\rho(\mathbf{r}_c)$
Ca-O6	2.3141 (4)	1.155	0.24	−0.88	6.46	4.68
Ca-O7	2.3512 (3)	1.161	0.30	−1.29	6.91	4.34
Ca-O60	2.3519 (4)	1.213	0.25	−1.06	5.84	3.72
Ca-O2	2.4932 (2)	1.269	0.21	−0.75	4.54	3.04
Ca-O3	2.5074 (2)	1.233	0.20	−0.51	3.92	2.90
Ca-O4	2.5316 (2)	1.284	0.18	−0.55	3.85	2.76
Ca-O20	2.6062 (2)	1.291	0.19	−0.61	3.55	2.33
Ca-O600	2.321 (1)	1.128	0.24	−0.91	6.45	4.62
Ca-O70	2.3518 (7)	1.153	0.29	−1.33	6.83	4.19
Ca-O60	2.357 (1)	1.150	0.29	−1.47	7.57	4.62
Ca-O4	2.4990 (6)	1.237	0.21	−0.67	4.39	3.06
Ca-O200	2.4996 (6)	1.273	0.19	−0.61	4.87	3.66
Ca-O300	2.5001 (5)	1.219	0.20	−0.74	4.48	2.99
Ca-O20	2.5394 (6)	1.295	0.16	−0.48	3.96	3.01
	⟨2.4445⟩	⟨1.219⟩	⟨0.226⟩	⟨−0.85⟩	⟨5.26⟩	⟨3.57⟩

r_b(O) increases linearly from 1.25 Å to 1.50 Å for the NaO bond and from 1.15 Å to 1.30 Å for the CaO bond (Fig. 6b) as both bonds increase ($r^2 \sim 0.85$) in length from ~2.3 to ~2.7 Å. Also, λ_3 and $\nabla^2\rho(\mathbf{r}_c)$ are highly correlated ($r^2 \sim 0.80$) with the bond lengths (Fig. 6c, d), both increasing with decreasing bond length (Hill et al. 1997). In addition, the bcp properties $\rho(\mathbf{r}_c) = 0.06$ eÅ^{-3}, r_b(O) = 1.42 Å and $\nabla^2\rho(\mathbf{r}_c) = 1.45$ eÅ^{-5} calculated by Hill et al. (1997) for an NaO bond length of 2.56 Å are in close agreement with those observed in this study (0.08 eÅ^{-3}, 1.45 Å, 1.48 eÅ^{-5}, respectively) for an NaO bond of the same length.

For purposes of comparison with the observed bcp properties of the CaO bonds, the geometries of the molecules Li_6CaO_4 (T_d point symmetry) and $Be_2Li_6CaO_6$ (D_{2d} point symmetry) were optimized. Using the wavefunctions generated in the calculations, electron density distributions were calculated and the bcp properties were evaluated. As expected, the trends between R(CaO) and the bcp properties for the CaO bonds are in the same direction as those observed above. The minimum energy CaO bond length (2.50 Å) calculated for the CaO_6 octahedron of the $Be_2Li_6CaO_6$ molecule falls within the range of the CaO bond lengths observed for the zeolites. Moreover, also the bcp properties, $\rho(\mathbf{r}_c) = 0.22$ eÅ^{-3}, r_b(O) = 1.27 Å, $|\lambda_{1,2}| = 0.65$ eÅ^{-5}, $\lambda_3 = 4.48$ eÅ^{-5}, and $\nabla^2\rho(\mathbf{r}_c) = 3.68$ eÅ^{-5}, calculated for the molecule are in reasonable agreement with the results obtained for the zeolites. They also agree with values recently calculated for danburite [$\rho(\mathbf{r}_c) = 0.21$ eÅ^{-5}, r_b(O) = 1.23 Å, $|\lambda_{1,2}| = 0.84$ eÅ^{-5}, $\lambda_3 = 4.97$ eÅ^{-5} and $\nabla^2\rho(\mathbf{r}_c) = 3.28$ eÅ^{-5}; G.V. Gibbs et al., in preparation].

Bond critical point in situ electronegativity

For the atoms of a given row of the periodic table, Pauling (1937) has demonstrated that this thermochemically based electronegativities, χ, increase from left to right in the table whereas they decrease with a few exceptions, from top to bottom within a given column. In addition, χ for a given atom was treated as single valued property that is independent of an atom's environment in either a molecule or a crystal. Studies have since suggested, however, that it may depend on the charge and the hybridization state of an atom (Hinze et al. 1963; Bergmann and Hinze 1996; Mullay 1987). For example, it has been argued that the electronegativity of the valence orbitals of C tends to increase as the orbital states change from sp^3 to sp^2 to sp simply because s-type orbitals are lower-lying in energy than the p-type orbitals (Allen 1989). Hill et al. (1997) have since defined the in situ electronegativity (Allen 1989) of an M atom, χ_M, in an oxide molecule in terms of the bcp properties of each of its MO bonds by the expression:

$$\chi_M = 1.31 \times \{[N_M \times \rho(\mathbf{r}_c)]/[r_b(O)]\}^{0.23} ,$$

where N_M is the number of valence electrons on M (Boyd and Edgecombe, 1988). They found that the χ_M values calculated for a given M-cation in the molecules agree, on average, with Pauling's values to within 5 and 10%. Also, the χ_M values were found to be highly correlated with the curvatures of $\rho(\mathbf{r}_c)$ and $\nabla^2\rho(\mathbf{r}_c)$. It was also found that χ_M increases with decreasing bond length. In particular, not only was it found that the electronegativities of Si and Ge both increase with decreasing bond length, coordination number, and increasing s-character, but that Ge is more electronegative than Si (Gibbs et al. 1998), as concluded earlier by Allred and Rochow (1958) and Allen (1989).

The in situ electronegativity values, χ_{Si}, calculated for the Si cations in the three zeolites (Tables 3–5) range between 1.72 and 1.96 with an average value of 1.85, compared with 1.75 obtained for the oxide molecules studied by Hill et al. (1997) and Pauling's value of 1.8. χ_{Si} is plotted against R(SiO), r_b(O), $\lambda_{1,2}$ and $\nabla^2\rho(\mathbf{r}_c)$ in

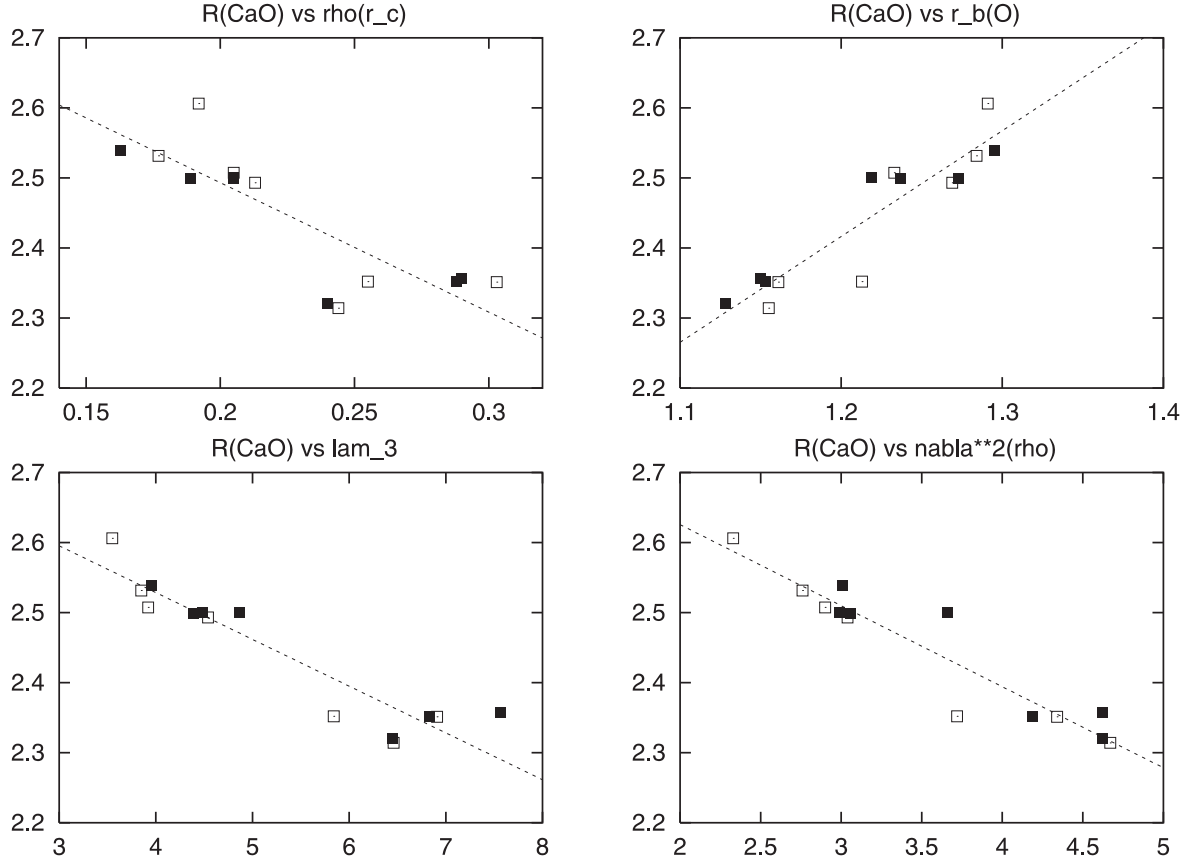

Fig. 6a–d Bond lengths and bcp properties of the CaO bonds in mesolite (*full squares*) and scolecite (*open squares*). **a** R(CaO) vs. $\rho(\mathbf{r}_c)$ (*top left*). **b** R(CaO) vs. r_b(O) (*top right*). **c** R(SiO) vs. λ_3 (*bottom left*). **d** R(CaO) vs. $\nabla^2\rho(\mathbf{r}_c)$ (*bottom right*)

Fig. 7. Not only is each correlation statistically significant, but each is consistent with the trends described for oxide and nitride molecules (Hill et al. 1997; Feth et al. 1998). As χ_{Si} increases, all of the above properties tend to decrease with chemical expectations. The χ_{Si} values calculated for the Al cations of the zeolites are smaller, ranging between 1.37 and 1.66 with an average value of 1.54 compared with 1.5 obtained by both Pauling (1937) and Hill et al. (1997). Unlike the value of χ_{Si}, the χ_{Al} values recorded for the zeolites appear to be independent of the AlO bond length, but they correlate negatively with $|\lambda_{1,2}|$ and λ_3 and positively with $\nabla^2\rho(\mathbf{r}_c)$. The negative correlation between χ_{Al} and $\nabla^2\rho(\mathbf{r}_c)$ conforms with those observed for the molecules. In contrast, the correlations for the molecules between χ_{Al} and $|\lambda_{1,2}|$ and λ_2 are both positive.

Concluding remarks

The trends between bond lengths and the bcp properties of the electron density distributions generated for a model structure of coesite and a variety of oxide molecules serve as useful guides for interpreting experimental electron density distributions in crystals. As derived in the model calculations, the value of the experimental electron density distribution at the bond critical points, the curvatures, and the Laplacian of the distribution tend to increase with decreasing bond length for a variety of crystals. Also, the bonded radius of the oxide anion tends to decrease with decreasing bond length and increasing electronegativity of the cation bonded to the anion (Bader 1990; Feth et al. 1993); it decreases in the order ~1.45, ~1.40, ~1.21, ~1.02, ~0.99, and ~0.95 Å when the oxide anion is bonded to K, Na, Ca, Al, B, and Si, respectively. This trend conforms with theoretical calculations discussed above that indicate r_b(O) decreases linearly with decreasing bond length, from the ionic radius of the oxide anion (1.45 Å) when bonded to the K cation to the atomic radius of the oxygen atom (0.65 Å when bonded to N (G.V. Gibbs et al., in preparation; see also Hill et al. 1997). The range of observed bonded radii indicates that the oxide anions in the zeolites are highly polarized as observed for danburite (Downs and Swope 1992; Gibbs et al. 1992). In addition, the values of $\rho(\mathbf{r}_c)$ and r_b(O) generated in the model calculations agree, for the most part, with those observed to within a few percent. However, the agreement is poorer, as expected, for such second derivative properties as the curvatures and the Laplacian of $\rho(\mathbf{r}_c)$. The experimental values of the electron density along the bonds increase in a regular way with the electronegativity of the cation: KO ~0.08 eÅ^{-3}; NaO, ~0.12 eÅ^{-3}; CaO, ~0.22 eÅ^{-3}; BeO, ~0.55 eÅ^{-3}; AlO, ~0.60 eÅ^{-3}; SiO, ~1.00 eÅ^{-3}, and BO, ~1.05 eÅ^{-3}. This result supports the argument that the value of $\rho(\mathbf{r}_c)$ coupled with the length of the bond is a direct measure of bond character; the larger the value of $\rho(\mathbf{r}_c)$ and the shorter the bond, the greater the covalent character of the

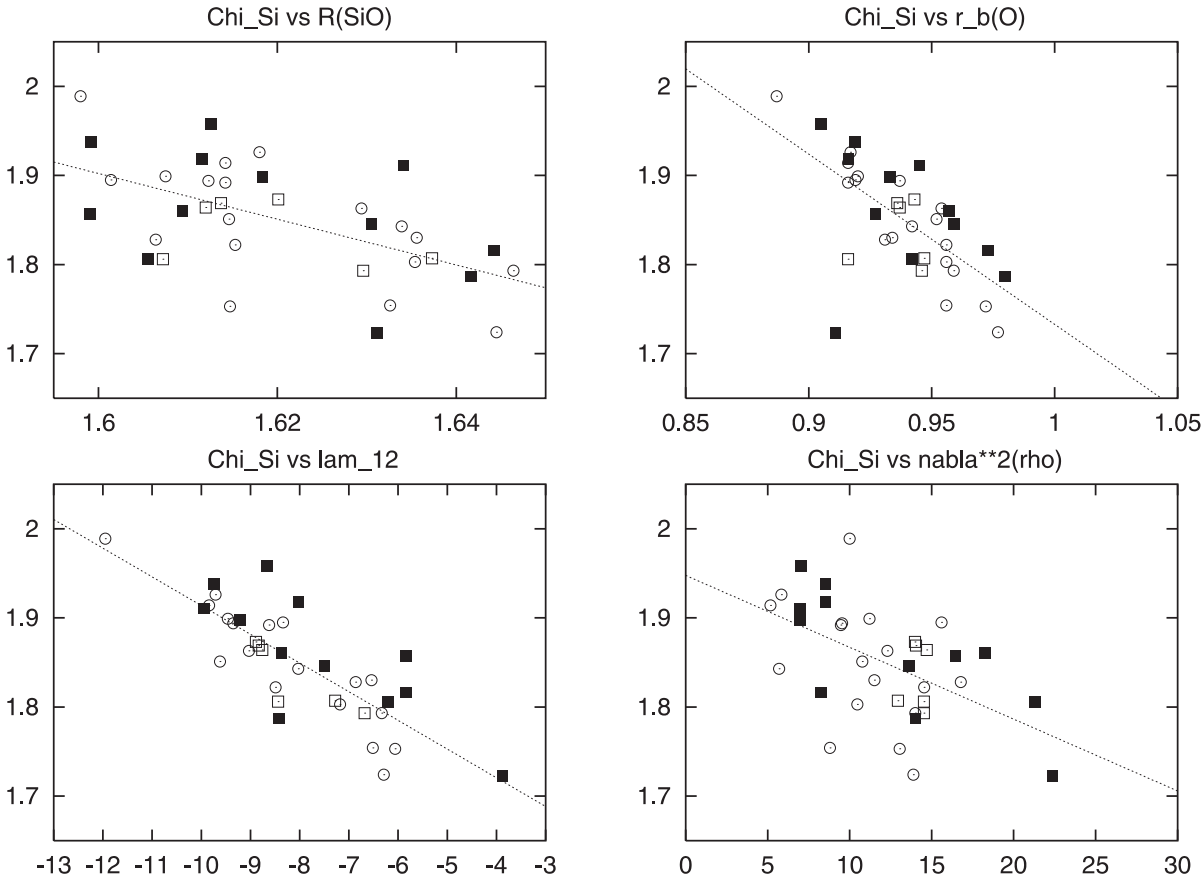

Fig. 7a–d In situ χ_{Si} and bcp properties of the SiO bonds in natrolite (*squares*), mesolite (*circles*), and scolecite (*full squares*). **a** χ_{Si} vs. R(SiO) (*top left*). **b** χ_{Si} vs. r_b(O) (*top right*). **c** χ_{si} vs. $\lambda_{1,2}$ (*bottom left*). **d** χ_{Si} vs. $\nabla^2\rho(\mathbf{r}_c)$ (*bottom right*)

bonded interaction (Gibbs et al. 1999a). The relatively large $\rho(\mathbf{r}_c)$ values observed for the SiO and BO bonds indicate that both are intermediate in character between ionic and covalent whereas the longer KO, NaO, CaO, BeO, and AlO bonds qualify as predominantly ionic on the basis of their $\rho(\mathbf{r}_c)$ values (Hill et al. 1997; Gibbs et al. 1999a). With decreasing bond length and increasing covalent character, the electron density along the bond path of each of these bonds tends to increase; the longer the bond, the greater the relative increase for a given change in bond length. Accompanying this increase, the curvatures of the electron density distribution both perpendicular and parallel to the bond path increase as the stationary point along the path migrates toward the oxide anion at a faster rate than it does toward the cation. Similar trends have likewise been found to hold for the electron density distributions and the bcp properties calculated for a relatively large number of minerals (G.V. Gibbs et al., in preparation).

Finally, it is puzzling why the correlations between R(SiO) and R(AlO) and $\rho(\mathbf{r}_c)$ are either poorly developed or lacking for the zeolites and related materials while they are well developed for topaz. It is also puzzling why R(CaO) is highly correlated with its bcp properties. It is not clear whether these observations are related to the relatively wide range of bond lengths observed for the CaO bond or to the difficulty of retrieving second derivative properties for experimentally generated distributions of $\rho(\mathbf{r})$. Given the strong correlations obtained for topaz (Ivanov et al. 1998), it appears that the latter is more likely true. Nonetheless, a study of the theoretical electron density distributions and the bcp properties is currently under way at Virginia Tech for a wide range of earth materials with the goal of improving the understanding of the crystal chemistry of these materials at the atomic level. Calculations are also being completed in locating the critical point properties of the Laplacian distributions. Information provided by these calculations should serve not only to locate potential sites of electrophilic and nucleophilic attack but also to improve our understanding of the activation of surface and internal oxide anions in zeolites and other minerals.

As demonstrated by Bader et al. (1984) and Aray and Bader (1996), for example, a mapping of the $\nabla^2\rho(\mathbf{r})$ for an observed or a geometry optimized structure can be used to pinpoint local maxima (lumps) together with local minima (holes) in the VSCCs of the oxide anions, features that have been used as a basis for understanding acid-base reactions. According to Bader and MacDougall (1985), the approach of the reactants in a Lewis acid-base reaction can be predicted by aligning the

lumps in the VSCC of a base with the holes in the VSCC of an acid. Upon locating the lumps and holes in the VSCCs in a zeolite, a map of the sites of chemical activity can be constructed. Such maps are bound to be useful in delineating those regions that are potentially susceptible to electrophilic and nucleophilic attack (cf. Aray and Bader 1996 and references therein). In exploring this problem for microporous zeolites, first-principal calculations for natrolite are currently underway like those completed for low quartz (Gibbs et al. 1999a). By evaluating the electron density Laplacian distribution of the geometry-optimized structure, it is anticipated that the sites of reactivity will be delineated just as they have been delineated on the bridging and nonbridging oxides anions for the $H_6Si_2O_7$ molecule (Gibbs et al. 1999b).

Acknowledgements For A.K., financial support by the Deutsche Forschungsgemeinschaft (contract no Ki 198/6-1,2) is gratefully acknowledged. The National Science Foundation is thanked for supporting GVG with Grant EAR-9627458. G.V.G. completed part of this study at the Division of Minerals at CSIRO, Clayton, Australia; Drs. Ian Gray and Rod Hill are both thanked for their kind hospitality and support.

References

Allen LC (1989) Electronegativity is the average one-electron energy of the valence-shell electrons in ground-state free atoms. J Am Chem Soc 111:9003–9014

Allred AL, Rochow E (1958) A scale of electronegativity based on electrostatic force. J Inorg Nucl Chem 5:264–268

Aray Y, Bader RFW (1996) Requirements for activation of surface oxygen atoms in MgO using the Laplacian of the electron density. Surface Science 351:233–249

Artioli G, Smith JV, Kvick A (1984) Neutron diffraction study of natrolite, $Na_2Al_2Si_3O_{10}{\cdot}2H_2O$ at 20 K. Acta Cryst C40:1658–1662

Bader RFW (1998) A bond path: universal indicator of bonded interactions. J Phys Chem 102A:7314–7323

Bader RFW (1990) Atoms in molecules. Oxford Science Publications. Oxford

Bader RFW, Essén H (1984) The characterizations of atomic interactions. J Chem Phys 80:1943–1960

Bader RFW, MacDougall PJ (1985) Toward a theory of chemical reactivity based on charge density. J Am Chem Soc 107:6788–6795

Bader RFW, MacDougall PJ, Lau CDH (1984) Bonded and nonbonded charge concentrations and their relation to molecular geometry and reactivity. J Am Chem Soc 106:1594–1605

Bergmann D, Hinze J (1996) Electronegativity and molecular properties. Angew Chem Int Engl 35:150–163

Berlin T (1951) Binding regions in diatomic molecules. J Chem Phys 19:208–213

Boyd RJ, Edgecombe KE (1988) Atomic and group electronegativities from the electron density distributions of molecules. J Am Chem Soc 110:4182–4186

Clementi E (1965) Tables of atomic functions. IBM J Res Dev 9 (Suppl)

Coppens P, Leiserowitz L, Rabinovich D (1965) Calculation of absorption corrections for camera and diffractometer data. Acta Cryst 18:1035–1038

Cruickshank DWJ (1949) The accuracy of electron-density maps in X-ray analysis with special reference to dibenzyl. Acta Cryst 2:65–82

Downs JW (1991) Electrostatic properties of minerals from X-ray diffraction data: a guide for accurate atomistic models. In: Ganguly J (ed) Diffusion, atomic ordering, and mass transport. Advances in Physical Geochemistry, vol. 8. Springer Berlin Heidelberg New York

Downs JW (1995) The electron density distribution of coesite. J Phys Chem 99:6849–6956

Downs JW, Swope RJ (1992) The Laplacian of the electron density and the electrostatic potential of danburite, $CaB_2Si_2O_8$. J Phys Chem 96:4834–4840

Feth S, Gibbs GV, Boisen MB, Myers RH (1993) Promolecule radii for nitrides, oxides and sulfides. A comparison with effective ionic and crystal radii. J Phys Chem 97:11 445–11 450

Feth S, Gibbs GV, Boisen MB, Hill FC (1998) A study of the bonded interactions in nitride molecules in terms of bond critical point properties and relative electronegativities. Phys Chem Miner 25:234–241

Feynman RP (1939) Forces in molecules. Phys Rev 56:340–343

Ghermani NE, Lecomte C, Dusausoy Y (1996) Electrostatic properties in zeolite-type materials from high-resolution X-ray diffraction – the case of natrolite. Phys Rev B53:5231–5239

Gibbs GV, Prewitt CT, Baldwin KJ (1977) A study of the structural chemistry of coesite. Z Kristallogr 145:108–123

Gibbs GV, Spackman MA, Boisen MB (1992) Bonded and promolecule radii for molecules and crystals. Am Mineral 77: 741–750

Gibbs GV, Downs JW, Boisen MB (1994) The elusive SiO bond. SILICA. Reviews in mineralogy, vol. 29. Heaney PJ, Prewitt CT, Gibbs GV eds Chap. 10, American Mineralogist, Washington, DC, pp 331–368

Gibbs GV, Boisen MB, Hill FC, Tamada O, Downs RT (1998) SiO and GeO bonded interactions as inferred from the bond critical point properties of electron density distributions. Phys Chem Minerals 25:574–584

Gibbs GV, Rosso KM, Teter DM, Boisen MB, Bukowinski MST (1999a) Model structures and properties of the electron density distribution for low quartz at pressure: a study of the SiO bond. J Mol Struc 485:13–25

Gibbs GV, Tamada O, Boisen Jr MB, Hill FC (1999b) Laplacian and bond critical point properties of the electron density distributions of sulfide bonds: a comparison with oxide bonds. Am Mineral 84:435–446

Gibbs GV, Rosso KM, Teter DM, Boisen Jr MB, Bukowinski MST. Model structures and properties of the electron density distribution for coesite. J Phys Chem (submitted)

Hamilton WC (1965) Significance tests on the crystallographic R-factor. Acta Cryst 18:502–510

Hill FC, Gibbs GV, Boisen MB (1997) Critical point properties of electron density distributions for oxide molecules containing first and second row cations. Phys Chem Miner 24:582–596

Hinze J, Whitehead MA, Jaffe HH (1963) Electronegativity: II. Bond and orbital electronegativities. J Am Chem Soc 85:148–154

Ivanov YU, Belokoneva EL, Protas J, Hansen NK, Tsirelson VG (1998) Multipole analysis of the electron density in topaz using X-ray diffraction data. Acta Cryst B54:774–781

Joswig W, Bartl H, Fuess H (1984) Structure refinement of scolecite by neutron diffraction. Z Kristallogr 160:219–223

Kuntzinger S, Ghermani NE, Dusausoy Y, Lecomte C (1998) Distribution and topology of the electron density in an aluminsilcate compound from high-resolution X-ray diffraction data: the case of scolecite. Acta Cryst B54:819–833

Lehman MS, Larsen FK (1974) A method for location of the peaks in step-scan measured Bragg reflections. Acta Cryst A30: 580–584

Mullay J (1987) Estimation of atomic and group electronegativities. Structure and bonding, vol 66. Sen KD, Jorgensen CK (eds) Springer Berlin, Heidelberg, New York

Pauling L (1937) The nature of the chemical bond. Cornell University Press, Ithaca, NY, pp 450

Sasaki S (1989) Numerical tables of anomalous scattering factors calculated by the Cromer and Liberman's method. KEK Rep 88–14:1–45

Stewart RF, Spackman MA (1983) VALRAY users manual. Dept Chem, Carnegie-Mellon University, Pittsburgh

Stewart RF, Spackman MA, Flensburg C (1996) VALRAY96 reference manual ß-version 0.02. Center for Crystallogr. Studies, University of Copenhagen, Denmark

Stuckenschmidt E, Kirfel A (1999) The crystal structure of mesolite. Eur J Mineral (in press)

Stuckenschmidt E, Joswig W, Baur WH (1993) Natrolite, Part I: Refinement of high-order data, separation of internal and external vibrational amplitudes from displacement parameters. Phys Chem Miner 19:562–570

Stuckenschmidt E, Joswig W, Baur WH, Hofmeister W (1997) Scolecite, Part I: Refinement of high-order data, separation of internal and external vibrational amplitudes from displacement parameters. Phys Chem Miner 24:403–410

Waasmaier D (1997) Bestimmung der Elektronendichteverteilung in Zeolithen. Thesis, University of Wuerzburg, Germany

Waasmaier D, Kirfel A, Stuckenschmidt E, Baur WH (1997) Topologische Untersuchung der Elektronendichteverteilung in Natrolith, Skolezit und Mesolith. Eur J Mineral (Suppl) 9:376